ORIGINAL PAPER

Compressibilities along the magnetite–magnesioferrite solid solution

C. Melai[1] · T. Boffa Ballaran[1] · L. Uenver-Thiele[2] · A. Kurnosov[1] · A. I. Chumakov[3] · D. Bessas[3] · D. J. Frost[1]

Abstract

To calculate the thermodynamic properties of recently discovered high-pressure mixed valence iron oxides in the system Fe–Mg–O, information on the equation of state of precursor inverse spinel phases along the magnetite–magnesioferrite join is needed. The existing equation of state data, particularly for magnesioferrite, are in poor agreement and no data exist for intermediate compositions. In this study, the compressibility of nearly pure magnesioferrite as well as of an intermediate $Mg_{0.5}Fe^{2+}_{0.5}Fe^{3+}_2O_4$ sample have been investigated for the first time up to approximately 19 and 13 GPa, respectively, using single-crystal X-ray diffraction in a diamond anvil cell. Samples were produced in high-pressure synthesis experiments to promote a high level of cation ordering, with the obtained inversion parameters larger than 0.83. The room pressure unit cell volumes, V_0, and bulk moduli, K_{T0}, could be adequately constrained using a second-order Birch–Murnaghan equation of state, which yields $V_0 = 588.97$ (8) Å^3 and $K_{T0} = 178.4$ (5) GPa for magnesioferrite and $V_0 = 590.21$ (5) Å^3 and $K_{T0} = 188.0$ (6) GPa for the intermediate composition. As magnetite has $K_{T0} = 180$ (1) GPa (Gatta et al. in Phys Chem Min 34:627–635, 2007. https://doi.org/10.1007/s00269-007-0177-3), this means the variation in K_{T0} across the magnetite–magnesioferrite solid solution is significantly non-linear, in contrast to several other Fe–Mg spinels. The larger incompressibility of the intermediate composition compared to the two end-members may be a peculiarity of the magnetite–magnesioferrite solid solution caused by an interruption of Fe^{2+}–Fe^{3+} electron hopping by Mg cations substituting in the octahedral site.

Keywords Magnesioferrite · Fe-rich spinels · Compressibility · Crystal chemistry · Single-crystal X-ray diffraction

Introduction

AB_2O_4 minerals with the spinel-type structure include aluminates, ferrites and chromites that are found in metamorphic and igneous rocks of the Earth's crust and mantle. Besides their petrological importance as an indicator of the degree of partial melting (Dick and Bullen 1984), spinels are used extensively in geothermometry and oxybarometry, which has motivated significant studies on their thermodynamic properties and cation ordering (e.g. Jamieson and Roeder 1984; O'Neill and Wall 1987). The spinel structure consists of a cubic (Fd$\bar{3}$m) close-packed oxygen array with cations in tetrahedral (*T*) and octahedral (*M*) coordination (Hill et al. 1979). Their crystal chemistry can be described by the general formula $^{IV}(A_{1-x}B_x)^{VI}(A_xB_{2-x})O_4$, where *x* defines the inversion parameter describing the fraction of B-type cations in the tetrahedral site and hence the degree of cation ordering. Two ordered configurations can be found in spinels, one with *x* = 0 (normal spinel) and one with *x* = 1 (inverse spinel), whereas complete disorder is achieved when *x* = 2/3. The ordering/disordering process between tetrahedral and octahedral sites in the spinel structure is non-convergent since it does not give rise to a change in symmetry.

As Cr–Al spinels are typically only stable within the top 60 km (i.e. ~ 2 GPa) of the mantle (Robinson and Wood 1998), their elastic properties are not critical in the thermodynamic description of their phase relations. The discovery of numerous mixed valence iron oxides at pressures above approximately 6 GPa (Lavina et al. 2011; Lavina and Meng 2015), however, and the observation that these oxides form solid solutions with Mg (Uenver-Thiele et al. 2017a, b) have renewed interest in thermodynamic calculations to

✉ C. Melai
  caterina.melai@uni-bayreuth.de

1   Bayerisches Geoinstitut, Universität Bayreuth, 95440 Bayreuth, Germany

2   Institut für Geowissenschaften, Goethe-Universität Frankfurt, Altenhöferallee 1, 60438 Frankfurt am Main, Germany

3   ESRF-The European Synchrotron CS40220, F-38043 Grenoble Cedex 9, France

understand the Fe–Mg–O phase diagram (Myhill et al. 2016; Uenver-Thiele et al. 2018). To determine the thermodynamic parameters for such high-pressure oxides, the properties of the lower pressure precursor phases become important, which in the case of Fe–Mg–O oxides include the inverse spinels along the binary join magnetite–magnesioferrite. Furthermore, it has been recognized that ferropericlase inclusions in sublithospheric diamonds can contain exsolution of Fe_3O_4 magnetite—$MgFe_2O_4$ magnesioferrite spinels (Harte et al. 1999; Wirth et al. 2014; Kaminsky et al. 2015; Palot et al. 2016; Anzolini et al. 2020). Wirth et al. (2014), for example, found spinel exsolutions that were enriched in Fe compared to the surrounding ferropericlase and had a stoichiometry, $(Mg_{0.42}Fe_{0.56}Mn_{0.02})$ $[Fe_{1.94}Al_{0.03}Cr_{0.03}]$ O_4, very close to the magnesioferrite-magnetite solid solution, having a 50:50 mfr–mgt composition. This exsolution likely occurred from the initial Fe^{3+}-bearing ferropericlase as the pressure–temperature conditions within the diamond inclusions changed (Wirth et al. 2014; Anzolini et al. 2020). To produce thermodynamic models to understand the conditions at which this exsolution may have occurred, and hence learn something about the diamond transport history, requires knowledge of the equation of state (EoS) parameters along the magnetite–magnesioferrite solid solution.

Previous X-ray diffraction studies on magnetite–magnesioferrite spinels have been performed to investigate the state of cation ordering as a function of temperature and pressure (O'Neill et al. 1992; Antao et al. 2005a, b). However, as pressures approach the limit of magnetite–magnesioferrite stability, the elastic properties will have a much larger effect on their volumes than those resulting from cation ordering alone, particularly as the spinels become more ordered at higher pressures (Antao et al. 2005a; Turkin and Drebushchak 2005). Several studies have investigated the compressibility of the end-members Fe_3O_4 and $MgFe_2O_4$ (Mao et al. 1974; Wilburn and Bassett 1977; Finger et al. 1986; Nakagiri et al. 1986; Olsen et al. 1994; Gerward and Olsen 1995; Haavik et al. 2000; Andrault and Bolfan-Casanova 2001; Levy et al. 2004; Reichmann and Jacobsen 2004; Lazor et al. 2004; Rozenberg et al. 2007; Gatta et al. 2007; Greenberg et al. 2009). The results, however, provide a wide range of bulk modulus, K_{T0}, with values $155 < K_{T0} < 222$ GPa for magnetite and $170.5 < K_{T0} < 233$ GPa for magnesioferrite (see references in Table 1). Most of these previous studies were performed on powdered samples. In some cases, the phases themselves were poorly characterized, involved different states of cation ordering or contained further components. A few of the magnetite studies, however, have used single-crystal diffraction (Finger et al. 1986; Nakagiri et al. 1986; Reichmann and Jacobsen 2004; Gatta et al. 2007 in Table 1). The results of these studies are in better agreement, suggesting that this technique may be more accurate than powder X-ray diffraction, likely because the broadening of

reflections due to non-hydrostatic stresses can be monitored very carefully. The large discrepancies among the different studies result in uncertainties when calculating thermodynamic properties from the breakdown reactions of these phases. Moreover, no data on samples with mixed compositions along the magnetite–magnesioferrite solid solution are present in the literature (Table 1).

The aim of this study is to constrain the compressibility of magnesioferrite as well as to investigate the compression behaviour of the magnetite–magnesioferrite solid solution. To this end, two single crystals with the approximate stoichiometries $MgFe_2O_4$ and $Mg_{0.5}Fe_{0.5}^{2+}Fe_2^{3+}O_4$ were investigated employing single-crystal X-ray diffraction at ambient conditions and in diamond anvil cells at higher pressures. To obtain samples that were close to being fully ordered inverse spinels, single crystals were produced in high-pressure and high-temperature synthesis experiments, and recovered and characterized before the compression experiments.

Experimental methods

Sample synthesis and characterization

$MgFe_2O_4$ single crystals were produced in a Kawai-type, 1200 tonne Sumitomo multi-anvil press at the Bayerisches Geoinstitut using pre-synthesized magnesioferrite powder. Details concerning the synthesis of the starting material can be found in Uenver-Thiele et al. (2017b). The high-pressure experiment was performed using a Cr_2O_3-doped MgO octahedral pressure assembly with an 18 mm edge length and WC cubes with 11 mm truncations. The starting material was loaded in a welded Pt capsule together with a thin layer of PtO_2 to maintain oxidizing conditions during the experiment. This ensured the presence of only Fe^{3+} in the synthesized crystals and minimized Fe loss to the capsule. The experiment was performed at 5 GPa and 1300 °C for 8 h. Heating was achieved with a graphite furnace and the temperature was monitored by a W_3/Re_{97}-W_{23}/Re_{75} thermocouple with no pressure correction applied to the electromotive force. The run product (experiment S7645) consisted of black single crystals with cubic shapes having dimensions varying between 20 and 150 μm. A JEOL JXA-8200 electron microprobe (EMP) equipped with five wavelength-dispersive spectrometers at the Bayerisches Geoinstitut was used to determine the composition of the synthesized sample. Four polished grains were mounted in epoxy for the measurement. Forsterite, andradite and Fe_2O_3 were used as standards for Mg, Fe and O respectively, and a ZAF algorithm was used for matrix correction. Measurements were performed in wavelength-dispersive mode with a 15 kV accelerating voltage and 15 nA beam current. The analyses yielded a final stoichiometry of $Mg_{0.96(1)}Fe_{0.04(1)}^{2+}Fe_2^{3+}O_4$, i.e.

Table 1 EoS parameters for sample mfr and Fe50 in the present study are reported together with the literature data for the magnetite–magnesioferrite solid solution

This study	Sample	V_0 (Å^3)	K_{T0} (GPa)	K'_T	P_{max} (GPa)	P medium	P calibrant	Method
Mfr (BM2)	$Mg_{0.96(1)}Fe_{2.04(1)}O_4$	588.97 (8)	178.4 (5)	4	18.87	He	Ruby	SXRD
Mfr (BM3)	$Mg_{0.96(1)}Fe_{2.04(1)}O_4$	589.02 (9)	176 (2)	4.2 (2)	18.87	He	Ruby	SXRD
Fe50 (BM2)	$Mg_{0.50(1)}Fe_{2.50(1)}O_4$	590.21 (5)	188.0 (6)	4	12.76	Ne	Ruby	SXRD
Fe50 (BM3)	$Mg_{0.50(1)}Fe_{2.50(1)}O_4$	590.20 (5)	189 (3)	3.7 (5)	12.76	Ne	Ruby	SXRD
References	**Sample**	V_0	K_{T0}	K'_T	P_{max}	P medium	P calibrant	Method
Mao et al. (1974) (BM2)	Fe_3O_4	591.96	183 (10)	4	3.2	NaCl	NaCl	PXRD
Wilburn and Bassett (1977) (BM2)	Fe_3O_4	–	155 (12)	4	6.5	ME	Ruby	PXRD
Finger et al. (1986)	Fe_3O_4	–	186 (5)	4[a]	4.5	ME	Ruby	SXRD
	Fe_3O_4	–	183 (5)	5.6[a]	4.5	ME	Ruby	SXRD
Nakagiri et al. (1986)	Fe_3O_4	591.54 (6)	181 (2)	5.5 (15)	4.5	ME	Ruby	SXRD
Olsen et al. (1994)	Fe_3O_4	–	200 (20)	–	5.5	MA	NaCl	SPXRD
Gerward and Olsen (1995)	Fe_3O_4	–	215 (25)	7.5 (40)	25	–	–	SPXRD
Haavik et al. (2000) (BM2)	Fe_3O_4	591.96	217 (2)	4	30	N_2	–	SPXRD
Haavik et al. (2000) (BM3)	Fe_3O_4	591.96	222 (8)	4.1 (9)	30	N_2	–	SPXRD
Lazor et al. (2004)	Fe_3O_4	591.96	198.4	6.8	36	NaCl	NaCl	SPXRD
Reichmann and Jacobsen (2004)	Fe_3O_4	592.19 (3)	180 (1)	5.2 (4)	8.3	MEW	Quartz	SXRD
Gatta et al. (2007) (BM2)	Fe_3O_4	591.4 (1)	180 (1)	4	11	MEW	Ruby	SXRD
Gatta et al. (2007) (BM3)	Fe_3O_4	591.4 (1)	182 (4)	3.6 (8)	11	MEW	Ruby	SXRD
Rozenberg et al. (2007)	Fe_3O_4	591.62 (7)	180.6 (1.1)	4.33 (13)	20	He	Sm^{2+}	PXRD
Gerward and Olsen (1995)	$MgFe_2O_4$	–	233 (40)	4.1 (2)	37	–		SPXRD
Andrault and Bolfan-Casanova (2001) (BM2)	$MgFe_2O_4$	589.9	195 (17)	4	46	–	Gold	SPXRD
Levy et al. (2004)	$MgFe_2O_4$	591.4 (1)	181.5 (13)	6.32 (14)	34	N_2	Ruby	SPXRD
Greenberg et al. (2009) (BM2)	$MgFe_2O_4$	591.0 (2)	170.5 (8)	4	30	He	Ruby	SPXRD
Greenberg et al. (2009) (BM3)	$MgFe_2O_4$	590.7 (2)	179 (2)	3.3 (2)	30	He	Ruby	SPXRD

Pressure medium, pressure calibrant and analytical methods are indicated when available

MEW, methanol:ethanol:water = 16:3:1; ME, methanol:ethanol = 4:1; PXRD, powder X-ray diffraction; SXRD, single-crystal XRD; SPXRD, synchrotron powder XRD; MA, multianvil experiments

[a]Assumed values; standard deviations in the last digits are in parentheses

close to the end-member $MgFe_2O_4$ composition and is referred to as mfr hereafter.

Single crystals of $Mg_{0.5}Fe_{0.5}^{2+}Fe_2^{3+}O_4$ were produced using an 800 tonne Walker-type multi-anvil at the University of Frankfurt (Walker et al. 1990). The experimental setup and sample characterization are reported in Uenver-Thiele et al. (2017a). The synthesis was performed at 9 GPa and 1000 °C for 7 h. The recovered sample (M650) contained several black crystals with sizes between 30 and 150 μm. Quantitative chemical analyses yielded a stoichiometry of $Mg_{0.50(2)}Fe_{0.50(1)}^{2+}Fe_2^{3+}O_4$ (Uenver-Thiele et al. 2017a). This sample is hereafter referred to as Fe50.

Synchrotron Mössbauer source (SMS) spectroscopy

SMS spectra on the Fe50 sample were collected at the Nuclear Resonance beamline ID18 (Rüffer and Chumakov 1996) of the European Synchrotron Radiation Facility (ESRF) in Grenoble, using the Synchrotron Mössbauer Source described by Potapkin et al. (2012). In this system, the source of radiation and optical elements are optimized to provide an intense, highly monochromatic, collimated and stable X-ray beam of small cross section at the Mössbauer transition energy of 14.4 keV. In contrast to a radioactive source, the beam emitted by the SMS is fully resonant and fully polarized, has high brilliance and can be focused to a 10 μm × 10 μm spot. Before and after collection of the SMS spectrum of sample Fe50, the linewidth was controlled via acquisition of a spectrum of $K_2Mg^{57}Fe(CN)_6$, which consists of a single line. The velocity scale was ± 12 mm/s and calibrated using 25 μm thick natural-enriched α-iron foil. The spectrum was collected for 2 h and fitted using pseudo-Voigt line shapes and a first-order polynomial baseline with the MossA 1.01f software package (Prescher et al. 2012). The Mössbauer spectrum (Fig. 1) is dominated by three
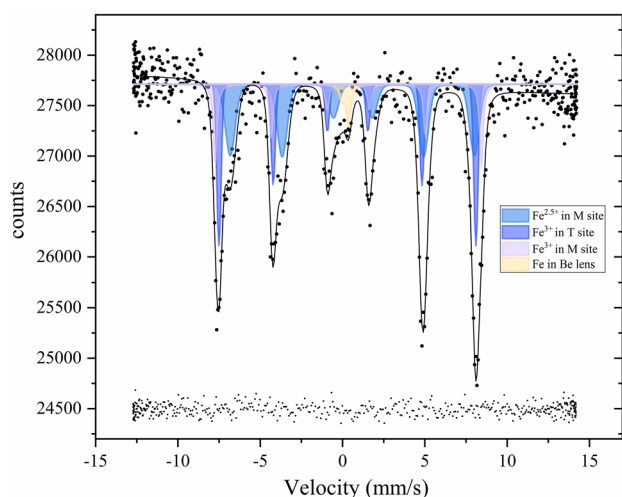
Fig. 1 Synchrotron Mössbauer source (SMS) spectrum of sample Fe50 collected at ambient conditions. Solid circles: experimental data; solid grey line: full transmission integral fit of the magnetic sextet shown in shaded coloured areas: Fe^{3+} at the tetrahedral site (dark blue); Fe^{3+} at the octahedral site (purple); $Fe^{2.5+}$ at the octahedral site (light blue) and Fe contained in the Be window (yellow). The fitting residual is shown at the bottom of the figure

sextets with the following hyperfine parameters: (1) centre shift (CS) = 0.30 (2) mm/s (relative to α-Fe) and hyperfine magnetic field (BHF) = 48.4 (1) T, which is characteristic of Fe^{3+} ions at the tetrahedral sites; (2) CS = 0.61 (4) mm/s and BHF = 45.9 (4) T, which can be assigned to an intermediate valence $Fe^{2.5+}$ at the octahedral sites; and (3) centre shift (CS) = 0.35 (5) mm/s and BHF = 50.1 (3) characteristic of octahedrally coordinated ferric iron (e.g. as typical for α-Fe_2O_3). A fourth component, observed in the SMS spectrum, is due to Fe contained in the beryllium (Be) lenses and is fit with known hyperfine parameters. The distribution of the iron species between the tetrahedral (T) and octahedral (M) site is $^TFe^{3+} = 33\%$; $^MFe^{3+} = 21\%$ and $^MFe^{2.5+} = 46\%$ with the $^MFe^{2.5+}$ component consisting of half $^MFe^{3+}$ and half $^MFe^{2+}$. No $^TFe^{2+}$ component could be fitted to the Mössbauer spectrum, suggesting that, if present, it is less than 5%, which is of the order of the uncertainties on the peak areas in the fitting procedure. Using the Mg and Fe concentrations from the microprobe analyses, together with the different iron components from the Mössbauer spectrum, the Fe50 chemical formula can be written as: $^T[Mg_{0.17(10)}Fe^{3+}_{0.83(10)}]$ $^M[Mg_{0.34(10)}Fe^{3+}_{1.09(10)}Fe^{2+}_{0.57(10)}]O_4$.

Single-crystal X-ray diffraction in air

Reflections from numerous single crystals from the Fe50 sample were examined, but all showed evidence of twinning to some extent. A Fe50 crystal (M650 × 7) with

dimensions of $50 \times 60 \times 70$ µm^3 was finally chosen for which one of the twin components was sufficiently small. This allowed the integration of an adequate number of reflections belonging only to the larger twin to be used for the structural refinements. For the mfr sample, it was possible to select a single crystal (S7645 × 8) with dimensions $70 \times 70 \times 80$ µm^3 that was devoid of twinning. Full intensity data collections for structural refinements at ambient conditions were performed in air for both samples, glued onto the tips of glass capillaries. Complete redundant intensity data were collected using an Oxford Xcalibur diffractometer equipped with a Sapphire 2 CCD area detector and a ceramic X-ray tube with MoKα radiation ($\lambda = 0.70784$ Å) monochromated using a graphite crystal and operating at 50 kV and 40 mA. Several ω scans were performed with a width of $0.5°$ and a default time of 10–20 s in a 2θ range between 2 and 78°. The intensity data were integrated with the Crysalis Pro software (Rigaku, Oxford diffraction) and Lorentz and polarization corrections as well as a numerical absorption correction based on the crystal shape were performed. Before integrating the intensity data of the Fe50 crystal, the Crysalis Pro software was used to determine the mutual orientation of the two twin components, which indicated a 60° rotation around [111], as expected for the spinel-type structure. The orientation matrices of the two twin components were then used to integrate the reflection intensities belonging to either one of the twin components, whereas overlapping reflections were neglected. This procedure resulted in 2848 reflections observed for the first twin component and 336 reflections observed for the second; therefore, only data from the first component were used for the structural analysis. The observed reflection conditions were consistent with the $Fd\bar{3}m$ space group; therefore, a structure solution and refinement based on F^2 were performed with the SHELX97 program package (Sheldrick 2008) in the ShelXle (Hübschle et al. 2011) graphical user interface using this space group. Scattering factors for neutral species (Ibers and Hamilton 1974) were employed for Mg, Fe and O, all sites were considered to be fully occupied and all atoms were refined anisotropically. Moreover, the occupancies of Mg and Fe were refined without chemical constraints both at the tetrahedral and octahedral sites. The magnesium and iron contents resulting from the refined occupancies are $^T[Mg_{0.02(3)}Fe_{0.98(3)}]^M[Mg_{0.44(3)}Fe_{1.56(3)}]$ O_4 for the Fe50 sample and $^T[Mg_{0.11(3)}Fe_{0.89(3)}]^M[Mg_{0.92(3)}Fe_{1.08(3)}]O_4$ for the mfr sample, in agreement with the chemical formula obtained from microprobe analyses. Details of the structural refinements are provided in the attached crystallographic information files (CIF). Unit-cell parameters, inversion parameters and bond lengths are reported in Table 2 together with data from the literature.

Table 2 Unit-cell parameter (a_0), composition and temperature of synthesis of the individual crystals along with the bond length distances for both the tetrahedral (T–O) and octahedral (M–O) sites and the inversion parameters (x)

Present study	Sample	T (°C) of synthesis	a (Å)	x	x calculated	T–O (Å)	M–O (Å)
S7645×8 (mfr)	$Mg_{0.96(1)}Fe_{2.04(1)}O_4$	1300 (5 GPa)	8.3821 (2)	0.85–0.89	0.89	1.9060 (19)	2.0442 (10)
M650×7 (Fe50)	$Mg_{0.50(1)}Fe_{2.50(1)}O_4$	1000 (9 GPa)	8.3883 (3)	> 0.83		1.898 (2)	2.0506 (13)
References	Sample	T (°C) of synthesis	a (Å)	x	x calculated	T–O (Å)	M–O (Å)
Antao et al. (2005b)	$Mg_{1.0003}Fe_{1.9998}O_4$**	900	8.39704 (5)	0.841 (4)	0.745	1.888 (3)	2.060 (1)
	Same sample as above***		8.39705 (5)			1.918 (4)	2.043 (2)
Levy et al. (2004)	$Mg_{1.02}Fe_{1.99}O_4$	1000 to 950 to 900	8.39389 (5)	0.802 (11)	0.775	n/a	n/a
Greenberg et al. (2009)	$MgFe_2O_4$	1200	8.3912 (7)	n/a	0.801	n/a	n/a
Antic et al. (2002)	$MgFe_2O_4$	500	8.3886 (1)	0.82 (1)	0.826	1.861 (2)	2.071 (2)
Andreozzi et al. (2001)	$Mg_{0.956}Fe_{2.044}O_4$	1200–800	8.3841 (3)		0.87	1.9099 (15)	2.0428 (8)
Nakatsuka et al. (2004)	$Mg_{1.02}Fe_{1.99}O_4$	1200–700–300	8.3600 (4)	0.854 (6)	1.100	1.915 (1)	2.031 (1)
Bosi et al. (2009)	Fe_3O_4	1200–900	8.3967 (3)	1.00		1.8872 (15)	2.0600 (8)
Fleet (1981)	Fe_3O_4	Natural	8.3941 (7)	n/a		1.888 (2)	2.0584 (9)
Finger et al. (1986)	Fe_3O_4	~1550 (*)	8.3778 (5)	n/a		1.887 (4)	2.054 (2)
Gatta et al. (2007)	Fe_3O_4	n/a	8.3950 (5)	n/a		1.885 (1)	2.0607 (8)
Haavik et al. (2000)	Fe_3O_4	1100	8.3965 (7)	n/a		1.889 (1)	2.059 (1)
Nakagiri et al. (1986)	Fe_3O_4	1050	8.3949 (3)	n/a		1.8873 (29)	2.059 (16)
Reichmann and Jacobsen (2004)	$(Fe_{2.996}Al_{0.003}Ti_{0.001})O_4$	Natural	8.39639 (14)	n/a		n/a	n/a

For comparison, literature data for the end-members magnesioferrite and magnetite are also shown.

[*]Temperature of synthesis was assessed from the work of Smiltens (1952) referenced in the methodology-related paper by Harrison and Aragon (1978); **data from the synchrotron; ***data from an in-house diffractometer for the same sample as in **. The uncertainties are reported in parenthesis. The values in the x calculated column were obtained using the relationship between lattice parameter and inversion parameter reported by O'Neill et al. (1992)

Diamond anvil cell (DAC) preparation

For the high-pressure experiments, the mfr and the Fe50 crystals were polished on one side to final dimensions of $60 \times 40 \times 20$ μm³ and $70 \times 55 \times 16$ μm³, respectively. The crystals were loaded onto two separate DACs equipped with Boehler-Almax diamonds with a culet size of 400 μm (Boehler and De Hantsetters 2004; Kantor et al. 2012). Samples were placed in the centre of a 250 μm hole that was drilled in pre-indented rhenium (Re) gaskets together with 10 μm diameter ruby spheres for pressure calibration. The two cells were loaded with different pressure transmitting media using the gas loading system installed at BGI (Kurnosov et al. 2008) and the pressure was increased to different target pressures. The cell with sample mfr was loaded with helium (He) at a starting pressure of 0.3 GPa and compressed in steps of ~1 GPa up to 18.87 (5) GPa. Above this pressure, broadening (assessed at full width half maximum) of the sample reflections was observed (Fig. 2) and the experiment was concluded. The cell with sample Fe50 was loaded with neon (Ne) and unit-cell lattice parameters were obtained in a first run (Run 1) up to 2.28 (2) GPa. Above this pressure, the gasket weakened and therefore a further loading with the same
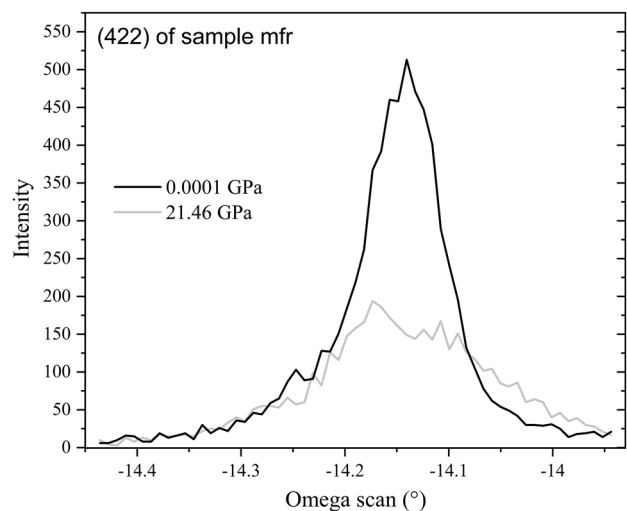

Fig. 2 The (422) reflection of the mfr sample is shown both at 0.0001 GPa (black solid line) and 21.46 GPa (light-grey solid line). Due to the onset of peak broadening at full width half maximum, as a result of non-hydrostatic conditions, the experiment was concluded and this pressure point was excluded from the fitting procedure

crystal in Ne was performed. Unit-cell parameters were then collected up to a maximum pressure of 12.76 (4) GPa (Run 2), after which reflection broadening occurred. After each pressure increase, the pressure inside the cell was left to stabilize for at least 1 day to minimize pressure changes during measurements. A Raman microspectrometer equipped with an He–Ne laser ($\lambda = 632.8$ nm) with 20 mW laser power was used to measure the fluorescence bands of the ruby sphere inside the DAC before and after the X-ray diffraction measurements. As a reference, a ruby chip at ambient conditions was also measured after each measurement. Pressures were determined using the ruby fluorescence calibration reported by Dewaele et al. (2008).

High-pressure single-crystal X-ray diffraction

High-pressure single-crystal diffraction for sample Fe50 was performed using a Huber four-circle diffractometer equipped with a Eulerian cradle goniometer, a point detector and a collimated diffracted beam from a conventional glass X-ray tube operating at 50 kV and 40 mA and producing MoKα radiation. Sample mfr was measured using a Huber four-circle Eulerian cradle diffractometer equipped with a point detector and using a high-brilliance rotating anode X-ray source with MoKα radiation operated at 55 kV and 45 mA and focused using multilayer VaryMax™ optics (Trots et al. 2011). For both samples, up to 16 Bragg reflections were centred using the eight-position centring method (King and Finger 1979). The centring procedure and the least-square refinement of the unit-cell parameters were performed using the SINGLE software (Angel and Finger 2011). The resulting unit-cell edge and volumes measured at different pressures are reported in Table 3.

Results and discussion

Degree of order of the investigated samples

The cation distribution at the octahedral and tetrahedral sites obtained by means of single-crystal X-ray diffraction can be used to calculate the bond distances of these sites using the structure model proposed by Lavina et al. (2002) based on 295 spinel single-crystal analyses from the literature. This model was tested to confirm whether all Fe present at the tetrahedral site in the mfr sample is trivalent. The T–O bond distance according to Lavina et al. (2002) can be obtained as:

$$\text{T--O} = \sum_i {}^{IV}X_i\,{}^{IV}D_i + k_1\,{}^{IV}\text{Fe}^{3+},$$

where ${}^{IV}X_i$ are the chemical species at the tetrahedral site, ${}^{IV}D_i$ are the cation oxygen bond distances of each specific atom at the tetrahedral site and k_1 is an empirical coefficient which accounts for the fact that the T–O distances are longer than expected when Fe^{3+} is present at that site. The cation–oxygen distances ${}^{IV}D_{Mg}$, ${}^{IV}D_{Fe^{2+}}$, and ${}^{IV}D_{Fe^{3+}}$, as well as the k_1 coefficient were taken from Lavina et al. (2002). From the tetrahedral site occupancies determined in the mfr structural refinement, i.e. ${}^{IV}X_{Fe} = 0.89\,(3)$ and ${}^{IV}X_{Mg} = 0.11(3)$, it is possible to calculate two different T–O bond distances, one assuming that all iron at the tetrahedral site is ferric,

Table 3 Unit-cell parameters and unit-cell volumes (Å^3) determined by means of high-pressure single-crystal X-ray diffraction for Fe50 sample (number M650×4) and the end-member mfr sample (number S7645×7)

M650×4 (Fe50)			S7645×7 (mfr)		
P (GPa)	a (Å)	V (Å^3)	P (GPa)	a (Å)	V (Å^3)
Run 1			0.00010	8.3821 (2)	588.93 (4)
0.00010	8.3883 (3)	590.23 (7)	1.30 (6)	8.36293 (11)	584.89 (2)
0.50 (4)	8.3811 (2)	588.72 (5)	3.14 (5)	8.3357 (2)	579.21 (3)
1.58 (4)	8.3638 (2)	585.07 (5)	4.96 (5)	8.3094 (2)	573.74 (3)
2.28 (3)	8.3547 (3)	583.17 (6)	6.44 (5)	8.2885 (2)	569.41 (3)
Run 2			8.14 (5)	8.2648 (2)	564.55 (4)
0.00010	8.3883 (2)	590.23 (5)	9.15 (11)	8.2522 (2)	561.96 (5)
3.44 (12)	8.3424 (4)	580.59 (7)	12.21 (5)	8.2142 (2)	554.24 (5)
6.18 (9)	8.3028 (4)	572.37 (7)	14.03 (5)	8.1928 (2)	549.92 (4)
7.36 (5)	8.2881 (4)	569.34 (7)	15.87 (7)	8.1720 (3)	545.75 (5)
8.66 (5)	8.2712 (4)	565.86 (7)	17.25 (12)	8.1563 (4)	542.60 (7)
9.77 (5)	8.2565 (4)	562.84 (7)	18.87 (5)	8.1391 (4)	539.18 (7)
9.96 (9)	8.2548 (4)	562.50 (7)			
10.83 (7)	8.2459 (5)	560.67 (9)			
10.97 (9)	8.2425 (5)	559.99 (9)			
11.90 (7)	8.2310 (10)	557.64 (11)			
12.76 (5)	8.2208 (10)	555.58 (11)			

Standard deviations are in parentheses

yielding a T–O = 1.894 Å and the other assuming that the 0.04 Fe^{2+} atoms present in the mfr sample (see chemical formula based on EMP measurements) all occupy the T site, yielding a T–O = 1.898 Å. Both values are similar, albeit smaller than the refined T–O bond distance T–O = 1.9060 (19) Å (Table 2). The small difference between the two calculated T–O bond distances (well inside the model uncertainties) does not allow differentiating between a full Fe^{3+} occupancy or the presence of minor amounts of Fe^{2+} at the tetrahedral site. Therefore, based on the Lavina et al. (2002) model, the mfr inversion parameter, x, could, in principle, vary between 0.85 and 0.89. However, the mfr inversion parameter can also be calculated using the previously determined linear relationship between the inversion parameter and the unit-cell lattice parameter a_0, using the equation $x = 81.34 - 9.598\, a_0$ (Å) (O'Neill et al. 1992). From this relationship, we obtain an inversion parameter of $x = 0.89$ (Table 2) in excellent agreement with that obtained from the structural refinements, assuming all Fe at the tetrahedral site is ferric iron. Therefore, the mfr sample synthesized in this study has a high degree of order. Moreover, the degree of order of the mfr sample is higher after annealing at 5 GPa and 1300 °C than that of the magnesioferrite starting material (Uenver-Thiele et al. 2017a), which had $x = 0.837$ (according to its unit-cell lattice parameters) and was synthesized at 900 °C, at room pressure. This confirms that pressure favours cation ordering in these spinels, in agreement with the results reported by Turkin and Drebushchak (2005) and Antao et al. (2005a). In fact, the determined inversion parameter is in good agreement with parameters determined at a similar pressure and temperature by Antao et al. (2005a) for mfr [i.e. 0.906 (8)].

For sample Fe50, the SMS spectrum (Fig. 1) showed the presence of 0.83 atoms per formula unit (apfu) of ferric iron at the tetrahedral site. This value is smaller than the refined Fe value of 0.98 (3) obtained from the structural refinement; however, no Fe^{2+} can be detected at the tetrahedral site in the SMS spectrum, which therefore requires 0.17 apfu of Mg at the tetrahedral site to maintain a full site occupancy. Note also that the amount of Fe^{2+} at the octahedral site derived from the SMS spectrum is already 0.57 (10) apfu, i.e. the entire Fe^{2+} content expected in the Fe50 sample, according to the chemical analysis. The difference between the cation distributions obtained from the SMS spectrum and from the single-crystal structure refinements are likely due to the resolution of the two methods, which can be assessed from the uncertainties, which are much larger for the SMS data. The T–O = 1.899 Å bond distance for the Fe50 spinel calculated using the Lavina et al. (2002) model from the SMS cation distribution [$^{IV}X_{Fe^{3+}} = 0.83(10)$ and $^{IV}X_{Mg} = 0.17(10)$] is in agreement with the tetrahedral bond length obtained from the structural refinements (Table 2), whereas the T–O = 1.887 Å calculated

from the cation distribution from the structural refinement [$^{IV}X_{Fe^{3+}} = 0.98(3)$ and $^{IV}X_{Mg} = 0.02(3)$] is smaller than the observed value. Given that Lavina et al. (2002) report that their model appears to underestimate the T–O bond distance for ferrite spinels, even considering the empirical coefficient k_1, we can expect that the inversion parameter of sample Fe50 is larger than 0.83, confirming also that Fe50 is an almost completely inverse spinel, having a similar cation substitution as the mfr sample.

Crystal chemistry of the $MgFe_2O_4$–Fe_3O_4 solid solution

The room pressure crystal chemistry of the samples in this study can be investigated through a comparison with literature data on magnetite–magnesioferrite samples and, in particular, with those used in previous compressibility studies (Table 2). Unit-cell parameters for magnesioferrite from compressibility studies are quite varied and range from $a = 8.3841$ (3) to 8.3970 (5) Å, with one outlier sample having $a = 8.3600$ (4) Å (Nakatsuka et al. 2004). These samples (Table 2) have been synthesized at temperatures between 500 and 1200 °C, with some being quenched in a stepwise manner, which has thus affected the final degree of order that is probably the main cause of the unit-cell variation. The predictions by O'Neill et al. (1992) for the expected unit-cell parameters of fully ordered and disordered magnesioferrite are indicated in Fig. 3a. The sample of Nakatsuka et al. (2004) (Table 2) has a very small unit-cell parameter, not consistent with the other reported values, and lies well below the predicted fully ordered end-member. This may be caused by a degree of non-stoichiometry through the substitution of a maghemite γ-Fe_2O_3 component, which is expected to decrease the unit-cell parameter further (O'Neill et al. 1992). The mfr sample investigated in this study is at the lower end of the main cluster of values from the literature ($a = 8.3821$ (2) Å), and is, therefore, one of the most ordered samples examined to date, in line with the evidence presented in the previous section.

Reported magnetite end-member unit-cell parameters show a much smaller range in values, between 8.3941 (7) and 8.3967 (3) Å, consistent with all the samples being ordered inverse spinel. As opposed to mfr, magnetite cation disorder cannot, to our knowledge, be quenched as it results only from the movement of an electron. Only the study of Finger et al. (1986) reports a significantly smaller value ($a = 8.3778$ (5) Å), which is interpreted to be due to the presence of a γ-Fe_2O_3 maghemite component (Volenik et al. 1975), consistent with the high temperature synthesis from a liquid.

To investigate the behaviour of the magnetite–magnesioferrite solid solution, the unit-cell parameters (Table 2) are plotted as a function of the molar $Mg/(Mg + Fe^{2+})$
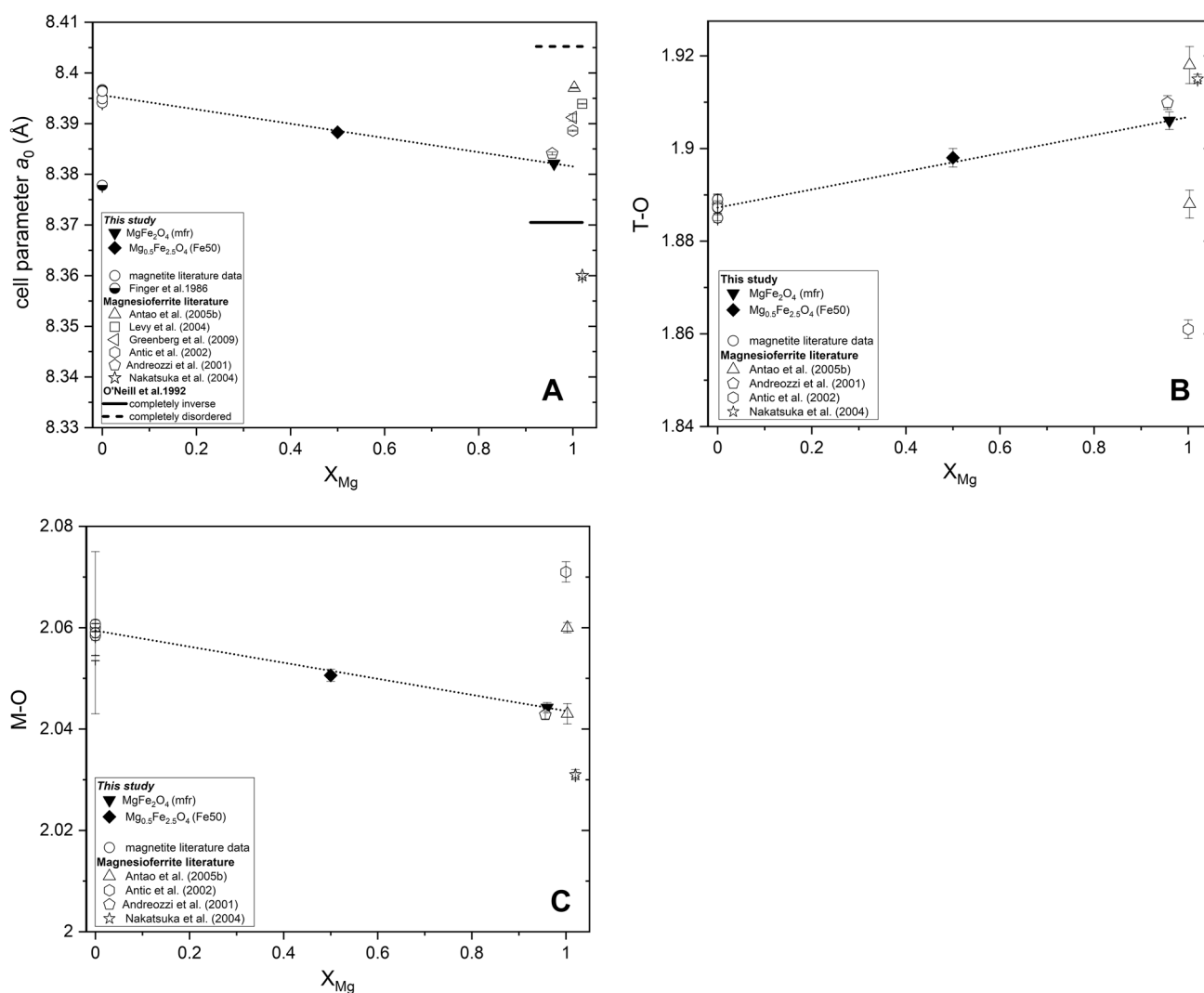
Fig. 3 A Variation of the unit-cell parameter (a_0) along the magnetite–magnesioferrite solid solution as a function of X_{Mg} (i.e. molar $Mg/(Mg+Fe^{2+})$). Predicted fully ordered (solid line) and fully disordered (dashed line) magnesioferrite unit-cell parameters (O'Neill et al. 1992) are also reported. **B** Tetrahedral, T–O bond length variation across the solid solution. **C** Octahedral, M–O bond length variation across the solid solution. Empty symbols refer to literature data (Table 2): circles are magnetite samples (Bosi et al. 2009; Fleet 1981; Finger et al. 1986 (half filled circle); Gatta et al. 2007; Haavik et al. 2000; Nakagiri et al. 1986) and for the magnesioferrite end-member, the different studies are reported in the legend. Filled symbols are the samples investigated in the present study: the triangle is the near end-member mfr sample and the diamond the intermediate $Mg_{0.5}Fe_{2.5}O_4$ sample (Fe50). The dashed line in all the plots connects the magnesioferrite end-member in the present study with an average value for the cluster of magnetite end-member samples reported in the literature (see "Results and discussion")

fraction, X_{Mg}, in Fig. 3a. A line has been drawn between the value obtained for mfr in this study and an average value ($a = 8.3962$ Å) for magnetite. The Fe50 sample investigated in this study lies on the linear trend between these most ordered samples. It should be noted, however, that it may be possible to produce a more ordered magnesioferrite sample, particularly at high pressures (Antao et al. 2005a), which would render a non-linear unit-cell relationship with Mg content, so there are no inferences from this line in terms of Vegard's law.

The Mg/Fe^{2+} substitution in the close-packed structure of spinels influences the tetrahedral, T–O, and octahedral, M–O bond lengths (Fig. 3b, c). In the ordered magnetite–magnesioferrite solid solution, Mg substitutes for Fe^{2+} at the octahedral site, whereas only Fe^{3+} occupies the tetrahedral site. With increasing Mg content, the M–O bond length decreases due to the smaller radius of Mg with respect to Fe^{2+}. This decrease causes a small increase of the tetrahedral bond distance, due to the close interconnectivity of the spinel structure. The magnetite samples reported in Table 2 have similar bond distance values, as expected due to their

high degree of order. A line through the average of these values and the bond distances of the mfr sample investigated in this study can be used to describe the linear behaviour of the most ordered magnetite–magnesioferrite solid solution. The M–O bond distance of the ordered Fe50 sample lies just slightly below this trend and the T–O bond length slightly above (Fig. 3b, c respectively). This very slight shortening of the M–O distance compared to the linear trend may be related to the raised incompressibility of this intermediate sample, as discussed later.

Cation disorder should decrease the M–O bond distances and increase the T–O bond distances even further, as Fe^{2+}/Mg enter the tetrahedral site and are replaced by Fe^{3+} at the octahedral site. This is clearly the case for the single-crystal $Mg_{0.956}Fe_{2.044}O_4$ sample studied by Andreozzi et al. (2001), which is slightly more disordered ($x = 0.87$) than our mfr sample. Data for the other reported end-member magnesioferrite samples (Table 2), however, do not appear to follow this behaviour (Fig. 3b, c) and show in some cases an increase in M–O distance even though they report higher levels of disorder. These studies, however, have been performed on polycrystalline samples and it is likely that the large correlations between refined parameters during the Rietveld refinements resulted in a poorly constrained oxygen positions due to its low scattering factor. This is well illustrated in the study by Antao et al. (2005b) where different values for the M–O and T–O bond distances are reported for the same sample analysed with two different X-ray sources (Table 2), despite that the same unit-cell lattice parameter is obtained from the two techniques.

Compressibility of the $MgFe_2O_4$–Fe_3O_4 solid solution

The decreasing trends of the unit-cell volumes with pressure for the mfr and Fe50 samples are shown in Fig. 4. No evidence of a phase transition was observed in the pressure range investigated. The end-member magnesioferrite is clearly more compressible than the Fe50 sample. The normalized stress, F_E, versus Eulerian finite strain, f_E, plot (Angel 2000) is illustrated in Fig. 5. Both data sets are well represented within uncertainties by horizontal straight lines indicating that a second-order truncation of the Birch–Murnaghan (BM) equation of state (EoS) (Birch 1947) is sufficient to describe the experimental P–V data. In this case, only two EoS parameters are refined, the room pressure unit-cell volume, V_0, and the bulk modulus, K_{T0}, whereas the first pressure derivative of the bulk modulus, K', assumes the value of four. The quality of the P–V data, however, appears adequate to constrain the value of K'; therefore, a third-order truncation of the BM EoS was also used, with three refined EoS parameters, V_0, K_{T0}, and K'. The results from fitting a BM2 and a BM3 EoS to the P–V data of both samples are reported in Table 1. The K' values of the BM3
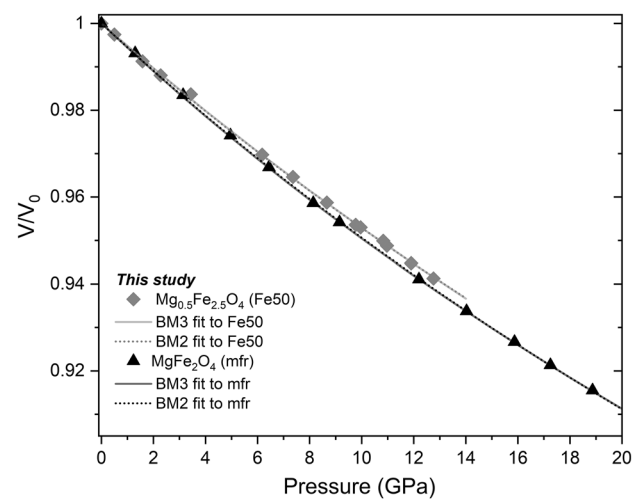

Fig. 4 Variation of the unit-cell volume as a function of pressure for the magnesioferrite (mfr) end-member and the intermediate $Mg_{0.5}Fe_{2.5}O_4$ (Fe50) crystals examined in this study. The solid lines show the fit of the third-order Birch–Murnaghan EoS (BM3) to the P–V data. Dashed lines show the fit of the second-order Birch-Murnaghan EoS (BM2). The standard uncertainties are smaller than the symbols
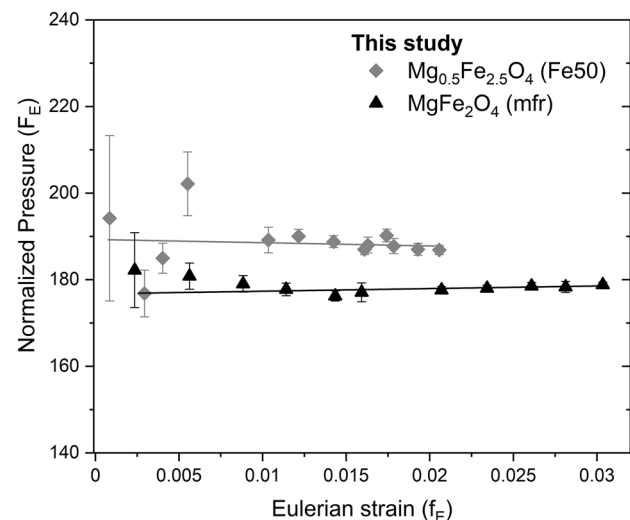

Fig. 5 Normalized pressure F_E versus the Eulerian strain f_E calculated for the P–V data collected in this study. Eulerian strain is defined as $[(V_0/V)^{2/3}-1]/2$ and F_E, and the normalized stress as $[P/((3f_E)*(1+2 f_E)^{5/2})]$ (Angel 2000). The solid lines are weighted linear regressions through the data points yielding intercept values of $K_{T0} = 176$ (2) GPa for the mfr near end-member magnesioferrite sample and $K_{T0} = 189$ (3) GPa for the Fe50 intermediate composition

EoS are identical to 4 within their uncertainties. K_{T0} is found to decrease significantly by approximately 10 GPa between the Fe50 (188.0 ± 0.6 GPa BM2) and mfr (178.4 ± 0.5 GPa BM2) samples (Fig. 6).

Data reported in the literature (Table 1) for the end-members magnetite and magnesioferrite vary considerably between the different studies (Fig. 6). For the magnesioferrite studies, K_{T0} values range between 170.5 and 233 GPa and K' between 3.3 and 6.32 (Fig. 6). The reasons for this large difference among the reported data sets are probably multiple, but likely include non-hydrostatic conditions and insufficient data coverage. A comparison between the inversion parameter x for the samples used in each study and the obtained EoS terms shows no obvious correlation. The very large K' in the study of Levy et al. (2004) probably results from non-hydrostatic conditions arising from the use of an N_2 pressure medium, which has been shown to become non-hydrostatic above approximately 6 GPa (Angel et al. 2007). The results of Greenberg et al. (2009) are very similar to those of this study up to approximately 20 GPa; however, their sample appears to become softer at higher pressures, leading to a low determined value of K' of 3.3. This can be seen in the F_E–f_E plot reported by Greenberg et al. (2009) which shows a kink above 20 GPa. Although somewhat speculative, one possible explanation for this would be the approach or commencement of a phase transition to a post-spinel phase, such as that observed by Andrault and Bolfan-Casanova (2001). As magnesioferrite is anyway expected to break down at ~ 10 GPa and high temperatures (Uenver-Thiele et al. 2017b), the measurements in the current study should cover a sufficient range (up to ~ 19 GPa) to obtain suitable elastic properties for thermodynamic calculations of its stability field.

Amongst various studies on magnetite compressibility, the study of Gatta et al. (2007) used a very similar methodology to that employed here and the results are in good agreement with several other studies on magnetite (Nakagiri et al. 1986; Rozenberg et al. 2007; Reichmann and Jacobsen 2004). As shown in Fig. 6, the K_{T0} value obtained for the mfr sample (178.4 (5) GPa) is only slightly lower than the value of 180 (1) GPa for magnetite (Gatta et al. 2007) while the values of K' obtained by using a BM3 EoS are identical within the uncertainties. That the values of K_{T0} for the two end-members are similar, with just a very small increase in K_{T0} between the Mg and Fe^{2+} end-members, is consistent with studies on the normal spinels $MgAl_2O_4$ (193 ± 1 GPa) and $FeAl_2O_4$ (193.9 ± 1.7 GPa; Nestola et al. 2007, 2015) and $MgCr_2O_4$ (182.5 ± 1.4 GPa) and $FeCr_2O_4$ (184.8 ± 1.7 GPa; Nestola et al. 2014). The sample with mixed composition (Fe50) is stiffer than both end-members (Fig. 7), indicating that a simple linear relationship of bulk moduli along the most ordered magnesioferrite–magnetite solid solution cannot describe the intermediate compositions. This behaviour is unusual, as other normal spinels such as Fe_2SiO_4–Mg_2SiO_4 (Higo et al. 2006) and $MgAl_2O_4$–$FeAl_2O_4$ (Bruschini et al. 2018) show near monotonous changes in K_{T0} across significant sections of the solid solutions. A non-linear behaviour has been observed for the bulk modulus along the $MgAl_2O_4$–$MnAl_2O_4$ join (Bruschini et al. 2015); however, the difference among the bulk moduli along the solid solution is less than 3 GPa (i.e. of the order of the uncertainties) and appears to be related to changes in the
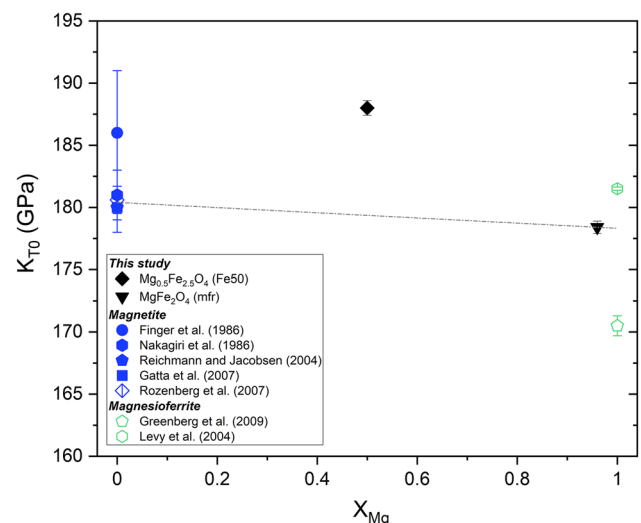

Fig. 6 K_{T0} versus K' plot showing the refined data of the studied samples and literature data on the magnetite–magnesioferrite solid solution. Black data points are the refined values for the two samples in the present study. Literature data are for magnetite (blue) and magnesioferrite (green). Filled symbols indicate data acquired using single-crystal X-ray diffraction. Empty symbols show data acquired with powder X-ray diffraction

Fig. 7 K_{T0} versus the Mg/(Mg + Fe^{2+}) ratio along the magnetite–magnesioferrite join. The dashed line joins the near-end-member magnesioferrite (mfr) K_{T0} value obtained in this study with the value for magnetite of 180 (1) GPa reported by Gatta et al. (2007). All K_{T0} values are for second-order truncations of the Birch–Murnaghan equation of state

inversion parameter (Bruschini et al. 2015). The difference between the K_{T0} of the Fe50 sample and its two end-members is also greater than the differences between any of the studied Fe–Mg spinel end-members.

One consideration is that although the magnetite is a fully ordered inverse spinel, the mfr and Fe50 samples retain some level of cation disorder ($x = 0.83$–0.89). If the fully ordered mfr were stiffer, this might render a linear X_{Mg}–K_{T0} relationship among the samples. Studies at least on the normal spinel $MgAl_2O_4$ appear to indicate that there is no resolvable effect of varying cation ordering on K_{T0} (Nestola et al. 2007; Bruschini et al. 2018). This implies that the potential softening effect of putting Mg into the octahedral site is balanced by the hardening influence of Al entering the tetrahedral site. However, the magnesioferrite inverse spinel may behave differently. The increase in volume at room temperature on disordering, for example, is larger for magnesioferrite compared to $MgAl_2O_4$ spinel (O'Neill et al. 1992; Nestola et al. 2007). Similarly, the softening effect of Mg entering the tetrahedral site may not be balanced by Fe^{3+} entering the octahedral site, as half of this site is already filled by Fe^{3+}. Density functional theory calculations on $MgAl_2O_4$ spinel (Núñez-Valdez et al. 2018) do predict a higher bulk modulus for a theoretically fully ordered inverse spinel, compared to normal ordered spinel. This effect is not predicted to be much larger, however, and is probably not sufficient to raise the mfr K_{T0} significantly to render a linear relationship between Mg substitution and K_{T0}.

The higher K_{T0} for the Fe50 sample implies that some type of Fe^{2+}–Mg interaction causes the octahedral site to be stiffer than when it is dominated by either Mg–Mg or Fe^{2+}–Fe^{2+} neighbours. One way that this might occur is through an interruption of the electron hopping between Fe^{2+} and Fe^{3+}, which causes the average $Fe^{2.5+}$ valence observed in Mössbauer spectra of magnetite. If the presence of local Mg reduces the extent of hopping, then the more localized Fe^{2+} 3d electron may increase the degree of covalency, and therefore the strength, of the Fe^{2+}–O octahedral bond. This could decrease the compressibility. Once the $X_{Mg} = 0.5$ composition has been reached, a further increase in Mg may then dilute this effect. If this is the case, then the non-linear elastic behaviour with composition is likely to be a peculiarity of the magnetite–magnesioferrite solid solution.

The polyhedral moduli in this system can be calculated using the ionic potential model of Bruschini et al. (2015), taking into account the state of cation ordering determined in this study, and can be used to obtain the bulk moduli (Bruschini et al. 2015) across the solid solution. However, this approach gives rise to end-member bulk moduli that are greater than the experimentally determined values and predicts a linear dependence of the bulk modulus across the solid solution. This also implies that the effect of Fe^{2+}

and Fe^{3+} cations on polyhedral compressibility of the spinel structure does not simply depend on their respective charge and ionic radii, as found for other spinel structures (Bruschini et al. 2015), but also on the specific types of metal–oxygen bonding.

A final aspect is to consider whether the change in incompressibility across the solid solution would result in a significant excess molar volume at high pressure, which could potentially contribute to the degree of non-ideality of the solid solution. At 10 GPa, however, i.e. near the limit of high-pressure magnetite–magnesioferrite stability, the predicted excess molar volume is at most 0.07 cm^3/mol, which would not have a significant influence on the thermodynamics of mixing.

Conclusions

In this study, the crystal chemistry and room temperature compressibility of near end-member $MgFe_2O_4$ magnesioferrite and an intermediate $Mg_{0.5}Fe_{2.5}O_4$ inverse spinel composition have been examined by means of single-crystal X-ray diffraction performed in the diamond anvil cell. A high degree of cation order was achieved by synthesizing the single-crystal samples at high-pressure and high-temperature conditions. The magnesioferrite sample synthesized at 5 GPa and 1300 °C had an inversion parameter of $x = 0.892$ (2), which is in good agreement with the high-pressure and high-temperature determinations of Antao et al. (2005a), and indicates a significant decrease in high-temperature disordering with increasing pressure. The intermediate sample, synthesized at 9 GPa and 1000 °C, was nearly fully ordered ($x > 0.83$).

Compressibility data were collected up to 18.87 GPa for magnesioferrite and up to 12.76 GPa for $Mg_{0.5}Fe_{2.5}O_4$. Plots of the normalized stress versus the Eulerian finite strain indicated that a second-order truncation of the Birch–Murnaghan equation of state would provide a suitable fit to the data. This yielded $V_0 = 588.97$ (8) $Å^3$ and $K_{T0} = 178.4$ (5) GPa for magnesioferrite and $V_0 = 590.21$ (5) $Å^3$ and $K_{T0} = 188.0$ (6) GPa for the $Mg_{0.5}Fe_{2.5}O_4$ composition. Using a third-order Birch–Murnaghan equation of state resulted in values of K' that were indistinguishable from 4, within the uncertainties. Measurements on magnetite using the experimental procedure of Gatta et al. (2007) reveal a $K_{T0} = 180$ (1) with $K' = 4$.

The slightly higher K_{T0} for the Fe end-member of the magnetite–magnesioferrite solid solution mimics the behaviour of the normal spinel joins $FeAl_2O_4$–$MgAl_2O_4$ and $FeCr_2O_4$–$MgCr_2O_4$ (Nestola et al. 2007, 2014, 2015). However, the significantly larger incompressibility of the intermediate $Mg_{0.5}Fe_{2.5}O_4$ composition has not been observed for other Fe–Mg spinels, but likely results from stiffer

octahedra, arising from some form of Fe^{2+}–Mg interaction. A smaller negative deviation from a linear compositional dependence of the octahedral M–O bond distance for the intermediate composition may be an indication for the stiffening of the octahedra, with respect to the end-members. A possible explanation is that the substitution of Mg into the octahedral site interrupts the exchange (hopping) of the Fe^{2+} $3d$ electron with neighbouring Fe^{3+} cations. If this electron is then more localized on the Fe^{2+} site, it may raise the covalency and, therefore, the strength of the Fe^{2+}–O bond, with a consequent increase of the incompressibility.

Declarations

Conflict of interest   The authors declare no conflict of interest.

References

Andrault D, Bolfan-Casanova N (2001) High-pressure phase transformations in the $MgFe_2O_4$ and Fe_2O_3–$MgSiO_3$ system. Phys Chem Miner 28:211–217. https://doi.org/10.1007/s002690000149

Andreozzi GB, Bosi F, Garramone F (2001) Synthetic spinels in the (Mg, Fe^{2+}, Zn) (Al, Fe^{3+})$_2O_4$ system. II. Preliminary chemical and structural data of hercynite and magnesioferrite samples. Periodico Di Mineralogia 70:193–204

Angel RJ, Finger LW (2011) SINGLE: a program to control single-crystal diffractometers. J Appl Crystallogr 44:247–251. https://doi.org/10.1107/S0021889810042305

Angel RJ, Bujak M, Zhao J, Gatta GD, Jacobsen SD (2007) Effective hydrostatic limits of pressure media for high-pressure crystallographic studies. J Appl Crystallogr 40:26–32. https://doi.org/10.1107/S0021889806045523

Angel RJ (2000) Equations of state. High-temperature and high pressure crystal chemistry, MSA. Rev Mineral Geochem 41:35–60. https://doi.org/10.2138/rmg.2000.41.2

Antao S, Hassan I, Crichton WA, Parise JB (2005a) Effects of high pressure and high temperature on cation ordering in magnesioferrite, $MgFe_2O_4$, using in situ synchrotron X-ray powder diffraction up to 1430 K and 6 GPa. Am Miner 90:1500–1505. https://doi.org/10.2138/am.2005.1797

Antao SM, Hassan I, Parise JB (2005b) Cation ordering in magnesioferrite, $MgFe_2O_4$, to 982 °C using in situ synchrotron X-ray powder diffraction. Am Miner 90:219–228. https://doi.org/10.2138/am.2005.1559

Antic B, Rodic D, Nikolic AS, Kacarevic-Popovic Z, Karanovi L (2002) The change of crystal symmetry and cation ordering in Li–Mg ferrites. J Alloy Compd 336:286–291. https://doi.org/10.1016/S0925-8388(01)01885-0

Anzolini C, Marquardt K, Stagno V, Bindi L, Frost DJ, Pearson DG, Harris JW, Hemley RJ, Nestola F (2020) Evidence for complex iron oxides in the deep mantle from FeNi(Cu) inclusions in superdeep diamond. Proc Natl Acad Sci USA 117:21088–21094. https://doi.org/10.1073/pnas.2004269117

Birch F (1947) Finite elastic strain of cubic crystals. Phys Rev 71:809–824. https://doi.org/10.1103/PhysRev.71.809

Boehler R, De Hantsetters K (2004) New anvil designs in diamond-cells. High Press Res 24:391–396. https://doi.org/10.1080/08957950412331323924

Bosi F, Halenius U, Skogby H (2009) Crystal chemistry of the magnetite-ulvospinel series. Am Miner 94:181–189. https://doi.org/10.2138/am.2009.3002

Bruschini E, Speziale S, Andreozzi GB, Bosi F, Hålenius U (2015) The elasticity of $MgAl_2O_4$–$MnAl_2O_4$ spinels by Brillouin scattering and an empirical approach for bulk modulus prediction. Am Miner 100(2–3):644–651. https://doi.org/10.2138/am-2015-4993

Bruschini E, Speziale S, Bosi F, Andreozzi GB (2018) Fe–Mg substitution in aluminate spinels: effects on elastic properties investigated by Brillouin scattering. Phys Chem Miner 45:759–772. https://doi.org/10.1007/s00269-018-0960-3

Dewaele A, Torrent M, Loubeyre P, Mezouar M (2008) Compression curves of transition metals in the Mbar range: experiments and projector augmented-wave calculations. Phys Rev B Condens Matter Mater Phys 78:104102-1–104113. https://doi.org/10.1103/PhysRevB.78.104102

Dick HJB, Bullen T (1984) Chromian spinel as a petrogenetic indicator in abyssal and alpine-type peridotites and spatially associated

lavas. Contrib Miner Petrol 86:54–76. https://doi.org/10.1007/BF00373711

Finger LW, Hazen RM, Hofmeister AM (1986) High-pressure crystal chemistry of spinel ($MgAl_2O_4$) and magnetite (Fe_3O_4): comparisons with silicate spinels. Phys Chem Miner 13:215–220. https://doi.org/10.1007/BF00308271

Fleet ME (1981) The structure of magnetite. Acta Crystallographica Section B: Structural Crystallography and Crystal Chemistry 37(4):917–920. https://doi.org/10.1107/S0567740881004597

Gatta GD, Kantor I, Boffa Ballaran T, Dubrovinsky L, McCammon C (2007) Effect of non-hydrostatic conditions on the elastic behaviour of magnetite: an in situ single-crystal X-ray diffraction study. Phys Chem Miner 34:627–635. https://doi.org/10.1007/s00269-007-0177-3

Gerward L, Olsen JS (1995) High-pressure studies of magnetite and magnesioferrite using synchrotron radiation. Appl Radiat Isot 46:553–554

Greenberg E, Rozenberg GK, Xu W, Arielly R, Pasternak MP, Melchior A, Garbarino G, Dubrovinsky LS (2009) On the compressibility of ferrite spinels: a high-pressure X-ray diffraction study of MFe_2O_4 (M = Mg Co, Zn). High Press Res 29:764–779. https://doi.org/10.1080/08957950903424424

Haavik C, Stølen S, Fjellvåg H, Hanfland M, Häusermann D (2000) Equation of state of magnetite and its high-pressure modification: thermodynamics of the Fe–O system at high pressure. Am Miner 85:514–523. https://doi.org/10.2138/am-2000-0413

Harrison HR, Aragon R (1978) Skull melter growth of magnetite (Fe_3O_4). Mater Res Bull 13:1097–1104. https://doi.org/10.1016/0025-5408(78)90195-2

Harte B, Harris JW, Hutchison MT, Watt GR, Wilding MC (1999) Lower mantle mineral associations in diamonds from São Luiz, Brazil. In: Fei E et al (eds) Mantle petrology: field observations and high pressure experimentation, a tribute to Francis R. Joe, Boyd, pp 125–153. https://doi.org/10.1007/978-81-322-1170-9_15

Higo Y, Inoue T, Li B, Irifune T, Liebermann RC (2006) The effect of iron on the elastic properties of ringwoodite at high pressure. Phys Earth Planet Inter 159:276–285. https://doi.org/10.1016/j.pepi.2006.08.004

Hill RJ, Craig JR, Gibbs GV (1979) Systematics of the spinel structure type. Phys Chem Miner 4:317–339. https://doi.org/10.1007/BF00307535

Hübschle CB, Sheldrick GM, Dittrich B (2011) ShelXle: a Qt graphical user interface for SHELXL. J Appl Crystallogr 44:1281–1284. https://doi.org/10.1107/S0021889811043202

Ibers JA, Hamilton WC (1974). In: Ibers JA, Hamilton WC (eds) International tables for X-ray crystallography: revised and supplementary tables to volumes 2 and 3. Kynoch Press, New York

Jamieson HE, Roeder PL (1984) The distribution of Mg and Fe^{2+} between olivine and spinel at 1300°C. Am Miner 69:283–291

Kaminsky FV, Ryabchikov ID, McCammon CA, Longo M, Abakumov AM, Turner S, Heidari H (2015) Oxidation potential in the Earth's lower mantle as recorded by ferropericlase inclusions in diamond. Earth Planet Sci Lett 417:49–56. https://doi.org/10.1016/j.epsl.2015.02.029

Kantor I, Prakapenka V, Kantor A, Dera P, Kurnosov A, Sinogeikin S et al (2012) BX90: a new diamond anvil cell design for X-ray diffraction and optical measurements. Rev Sci Instrum 83:125102. https://doi.org/10.1063/1.4768541

King HEJ, Finger LW (1979) Diffracted beam crystal centering and its application to high-pressure crystallography. J Appl Crystallogr 12:374–378. https://doi.org/10.1107/S0021889879012723

Kurnosov A, Kantor I, Boffa-Ballaran T, Lindhardt S, Dubrovinsky L, Kusnestov A, Zehnder BH (2008) A novel gas-loading system for mechanically closing of various types of diamond anvil cells. Rev Sci Instrum 79:045110. https://doi.org/10.1063/1.2902506

Lavina B, Meng Y (2015) Unraveling the complexity of iron oxides at high pressure and temperature: Synthesis of Fe_5O_6. Sci Adv 1:2–7. https://doi.org/10.1126/sciadv.1400260

Lavina B, Salviulo G, Della Giusta A (2002) Cation distribution and structure modelling of spinel solid solutions. Phys Chem Miner 29:10–18. https://doi.org/10.1007/s002690100198

Lavina B, Dera P, Kim E, Meng Y, Downs RT, Weck PF, Sutton SR, Zhao Y (2011) Discovery of the recoverable high-pressure iron oxide Fe_4O_5. Proc Natl Acad Sci USA 108:17281–17285. https://doi.org/10.1073/pnas.1107573108

Lazor P, Shebanova ON, Annersten H (2004) High-pressure study of stability of magnetite by thermodynamic analysis and synchrotron X-ray diffraction. J Geophys Res Solid Earth 109:B05201. https://doi.org/10.1029/2003JB002600

Levy D, Diella V, Dapiaggi M, Sani A, Gemmi M, Pavese A (2004) Equation of state, structural behaviour and phase diagram of synthetic $MgFe_2O_4$, as a function of pressure and temperature. Phys Chem Miner 31:122–129. https://doi.org/10.1007/s00269-004-0380-4

Mao H-K, Takahashi T, Bassett WA, Kinsland GL, Merrill L (1974) Isothermal compression of magnetite to 320 KB. J Geophys Res 79:1165–1170. https://doi.org/10.1029/JB079i008p01165

Myhill R, Ojwang DO, Ziberna L, Frost DJ, Ballaran TB, Miyajima N (2016) On the P–T–fO_2 stability of Fe_4O_5, Fe_5O_6 and Fe_4O_5-rich solid solutions. Contrib Miner Petrol 171:51. https://doi.org/10.1007/s00410-016-1258-4

Nakagiri N, Manghnani MH, Ming LC, Kimura S (1986) Crystal structure of magnetite under pressure. Phys Chem Miner 13:238–244. https://doi.org/10.1007/BF00308275

Nakatsuka A, Ueno H, Nakayama N, Mizota T, Maekawa H (2004) Single-crystal X-ray diffraction study of cation distribution in $MgAl_2O_4$–$MgFe_2O_4$ spinel solid solution. Phys Chem Miner 31:278–287. https://doi.org/10.1007/s00269-004-0385-z

Nestola F, Boffa Ballaran T, Balic-Zunic T, Princivalle F, Secco L, Dal Negro A (2007) Comparative compressibility and structural behavior of spinel $MgAl_2O_4$ at high pressures: the independency on the degree of cation order. Am Miner 92:1838–1843. https://doi.org/10.2138/am.2007.2573

Nestola F, Periotto B, Andreozzi GB, Bruschini E, Bosi F (2014) Pressure-volume equation of state for chromite and magnesiochromite: a single-crystal X-ray diffraction investigation. Am Miner 99:1248–1253. https://doi.org/10.2138/am.2014.4765

Nestola F, Periotto B, Anzolini C, Andreozzi GB, Woodland AB, Lenaz D, Alvaro M, Princivalle F (2015) Equation of state of hercynite, $FeAl_2O^4$, and high-pressure systematics of Mg–Fe–Cr–Al spinels. Mineral Mag 79:285–294. https://doi.org/10.1180/minmag.2015.079.2.07

Núñez-Valdez M, Bruschini E, Speziale S, Bosi F, Fregola RA, D'Ippolito V, Andreozzi GB (2018) Reexploring the cation ordering and magnetic cation substitution effects on the elastic anisotropy of aluminum spinels. J Appl Phys 124:175901. https://doi.org/10.1063/1.5050064

O'Neill HSC, Wall VJ (1987) The olivine-orthopyroxene-spinel oxygen geobarometer, the nickel precipitation curve, and the oxygen fugacity of the earth's upper mantle. J Petrol 28:1169–1191. https://doi.org/10.1093/petrology/28.6.1169

O'Neill HSC, Annersten H, Virgo D (1992) The temperature dependence of the cation distribution in magnesioferrite ($MgFe_2O_4$) from powder XRD structural refinements and Mossbauer spectroscopy. Am Miner 77:725–740

Olsen JS, Gerward L, Hinze E, Kremmler J (1994) High-pressure, high-temperature study of magnetite using synchrotron radiation. Mater Sci Forum 166–169:577–582. https://doi.org/10.4028/www.scientific.net/MSF.166-169.577

Palot M, Jacobsen SD, Townsend JP, Nestola F, Marquardt K, Harris JW, Stachel T, McCammon CA, Pearson DG (2016) Evidence for

H_2O-bearing fluids in the lower mantle from diamond inclusion. Lithos 265:237–243. https://doi.org/10.1016/j.lithos.2016.06.023

Potapkin V, Chumakov AI, Smirnov GV, Celse JP, Rüffer R, McCammon C, Dubrovinsky L (2012) The ^{57}Fe synchrotron Mössbauer source at the ESRF. J Synchrotron Radiat 19:559–569. https://doi.org/10.1107/S0909049512015579

Prescher C, McCammon C, Dubrovinsky L (2012) MossA: a program for analyzing energy-domain Mössbauer spectra from conventional and synchrotron sources. J Appl Crystallogr 45:329–331. https://doi.org/10.1107/S0021889812004979

Reichmann HJ, Jacobsen SD (2004) High-pressure elasticity of a natural magnetite crystal. Am Miner 89:1061–1066. https://doi.org/10.2138/am-2004-0718

Robinson JAC, Wood BJ (1998) The depth of the spinel to garnet transition at the peridotite solidus. Earth Planet Sci Lett 164:277–284. https://doi.org/10.1016/S0012-821X(98)00213-1

Rozenberg GK, Amiel Y, Xu WM, Pasternak MP, Jeanloz R, Hanfland M, Taylor RD (2007) Structural characterization of temperature- and pressure-induced inverse normal spinel transformation in magnetite. Phys Rev B Condens Matter Mater Phys 75:020102. https://doi.org/10.1103/PhysRevB.75.020102

Rüffer R, Chumakov AI (1996) Nuclear resonance beamline at ESRF. Hyperfine Interact 97–98:589–604. https://doi.org/10.1007/BF02150199

Sheldrick GM (2008) A short history of SHELX. Acta Crystallogr Sect A Found Crystallogr 64:112–122. https://doi.org/10.1107/S0108767307043930

Smiltens J (1952) The growing of single crystals of magnetite. J Chem Phys 20:990–994. https://doi.org/10.1063/1.1700664

Trots DM, Kurnosov A, Vasylechko L, Berkowski M, Boffa-Ballaran T, Frost DJ (2011) Elasticity and equation of state of $Li_2B_4O_7$. Phys Chem Miner 38:561–567. https://doi.org/10.1007/s00269-011-0428-1

Turkin AI, Drebushchak VA (2005) Cation distribution in $MgFe_2O_4$ vs. pressure and temperature: experiments in a "piston-cylinder" apparatus. Am Miner 90:764–767. https://doi.org/10.2138/am.2005.1714

Uenver-Thiele L, Woodland AB, Boffa Ballaran T, Miyajima N, Frost DJ (2017a) Phase relations of Fe–Mg spinels including new high-pressure post-spinel phases and implications for natural samples. Am Miner 102:2054–2064. https://doi.org/10.2138/am-2017-6119

Uenver-Thiele L, Woodland AB, Boffa-Ballaran T, Miyajima N, Frost DJ (2017b) Phase relations of $MgFe_2O_4$ at conditions of the deep upper mantle and transition zone. Am Miner 102:632–642

Uenver-Thiele L, Woodland AB, Miyajima N, Boffa-Ballaran T, Frost DJ (2018) Behaviour of Fe_4O_5–$Mg_2Fe_2O_5$ solid solutions and their relation to coexisting Mg–Fe silicates and oxide phases. Contrib Miner Petrol 173:1–16. https://doi.org/10.2138/am-2017-5871

Volenik K, Seberini M, Neid J (1975) A Mössbauer and X-ray diffraction study of nonstoichiometry in magnetite. Czech J Phys 25:1063–1071. https://doi.org/10.1007/BF01597585

Walker D, Carpenter MA, Hitch CM (1990) Some simplifications to multianvil devices for high pressure experiments. Am Miner 75(9–10):1020–1028

Wilburn DR, Bassett WA (1977) Isothermal compression of magnetite (Fe_3O_4) up to 70 kbar under hydrostatic conditions. High Temp High Press 9:35–39

Wirth R, Dobrzhinetskaya L, Harte B, Schreiber A, Green HW (2014) High-Fe (Mg, Fe)O inclusion in diamond apparently from the lowermost mantle. Earth Planet Sci Lett 404:365–375. https://doi.org/10.1016/j.epsl.2014.08.010